Internal gravity waves generated by subglacial discharge: implications for tidewater glacier melt

J. M. Cusack[1,2], R. H. Jackson[2], J. D. Nash[1], E. Skyllingstad[1], E. C. Pettit[1], D. A. Sutherland[3], R. J. Motyka[4,5], J M. Amundson[5]

[1]Oregon State University, College of Earth, Ocean and Atmospheric Sciences
[2]Rutgers, The State University of New Jersey
[3]University of Oregon
[4]University of Alaska Fairbanks
[5]University of Alaska Southeast

Key Points:

- First-ever time series of water velocity in the calving zone of a glacier terminus, enabled by moorings deployed from a robotic vessel.
- Energetic high-frequency internal waves were emitted from the subglacial discharge plume and reproduced in a large eddy simulation.
- Internal waves have the potential to significantly increase ambient melt rates by enhancing water velocity across the terminus.

Corresponding author: Jesse M. Cusack, jesse.cusack@oregonstate.edu

Abstract

Submarine melting has been implicated in the accelerated retreat of marine-terminating glaciers globally. Energetic ocean flows, such as subglacial discharge plumes, are known to enhance submarine melting in their immediate vicinity. Using observations and a large eddy simulation, we demonstrate that discharge plumes emit high-frequency internal gravity waves that propagate along glacier termini and transfer energy to distant regions of the terminus. Our analysis of wave characteristics and their correlation with subglacial discharge forcing suggest that they derive their energy from turbulent motions within the discharge plume and its surface outflow. Accounting for the near-terminus velocities associated with these waves increases predicted melt rates by up to 70%. This may help to explain known discrepancies between observed melt rates and theoretical predictions. Because the dynamical ingredients – a buoyant plume rising through a stratified ocean – are common to many tidewater glacier systems, such internal waves are likely to be widespread.

Plain Language Summary

Recent acceleration in sea-level rise has been attributed to the mass loss of glaciers that terminate in the ocean, such as those found in Greenland and Alaska. Warm ocean currents are thought to melt glacier ice, contributing to their loss of mass and retreat. We use moored instruments deployed with autonomous vehicles, as well as a computer simulation, to demonstrate how a previously unconsidered type of current, called an internal wave, is generated at marine-terminating glaciers. We show that the strength of the waves is related to the amount of subglacial discharge that originates from surface melting occurring at higher elevations on the glacier. Internal waves may contribute to local ice melt, and ultimately glacier mass loss, by mixing warm water in a thin layer immediately adjacent to the glacier.

1 Introduction

Fjords with active tidewater glaciers are principle conduits for meltwater runoff and ice discharge into the ocean. Tidewater glaciers have been losing mass in recent years and contributing to an acceleration in sea-level rise (Rignot & Kanagaratnam, 2006; Chambers et al., 2017; Mouginot et al., 2019; Shepherd et al., 2020). The ocean dynamics occurring within glacial fjords play a key role in modulating glacier retreat (Straneo & Cenedese, 2015; Wood et al., 2018). Ocean thermal forcing directly causes mass loss via melting and may also act to amplify other ice-loss mechanisms such as calving (Luckman et al., 2015; Slater et al., 2021), although there is uncertainty in the sign and magnitude of this effect (Ma & Bassis, 2019; Mercenier et al., 2020). Increasing meltwater runoff has been linked to a weakening of the Atlantic Meridional Overturning circulation in recent decades (Thornalley et al., 2018).

Since direct observations of submarine melting are scarce, melt rates are often estimated from near-terminus ocean velocity, temperature, and salinity using a parameterization for heat and salt fluxes through the ocean boundary layer. The most widely used form of the parameterization, known as the 3-equation model, assumes shear-driven boundary layer dynamics in which the heat and salt fluxes are linearly dependent on the terminus-parallel ocean velocity (Holland & Jenkins, 1999; Jenkins, 2011, and text S1). The 3-equation model suggests that the melt rate m is proportional to:

$$m \propto C_D^{\frac{1}{2}} \Gamma_T |\boldsymbol{u}| \Delta T, \tag{1}$$

where C_D is the drag coefficient, Γ_T is the turbulent thermal transfer parameter, $\boldsymbol{u}$ is the terminus-parallel outer boundary layer velocity, and ΔT is the temperature dif-

ference across the boundary layer. Parameterized melt rates are often coupled with theory for buoyant plumes (Morton et al., 1956; Jenkins, 2011) and have been used to model the melt rates of subglacial discharge plumes (Cowton et al., 2015; Slater et al., 2015; Carroll et al., 2016; Slater et al., 2022), which are highly-energetic buoyant flows commonly found at tidewater glaciers. These discharge plumes rise from the glacier grounding line and originate from upstream surface meltwater that has drained to the glacier bed and flowed downslope via a network of subglacial channels. Measurements of terminus morphology suggest that melt induced by discharge plumes is large (Fried et al., 2015; Rignot et al., 2015; Fried et al., 2019; Sutherland et al., 2019), consistent with solutions to Eq. (1) for high-velocity flows.

Away from the main subglacial discharge plume(s), coupled plume-melt theory suggests that the buoyant forcing from melt alone drives relatively weak plumes (Cowton et al., 2015; Straneo & Cenedese, 2015; Magorrian & Wells, 2016). As such, melting occurring away from discharge plumes, termed ambient melting, was thought to be small. Yet, the only direct observations of submarine melting made to date demonstrate that ambient melting exceeds theoretical estimates by one to two orders of magnitude (Sutherland et al., 2019). Reasons for this discrepancy include: incorrect values for the drag and turbulent transfer coefficients, an incorrect form of the parameterization at low velocity (McConnochie & Kerr, 2017; Schulz et al., 2022) and the neglect of non-plume flows from the assumed near-terminus ocean velocity, such as those from lateral fjord-circulation (Slater et al., 2018; Jackson et al., 2020). Here, we focus on additional sources of near-terminus currents that could contribute to enhancing melt, in particular, energetic internal waves revealed by a new set of observations.

Throughout the ocean, internal gravity waves are a dominant source of energy for turbulent mixing and exert significant influence over a diverse range of processes from nutrient availability to the global overturning circulation (Melet et al., 2013; MacKinnon et al., 2017; Woodson, 2018). Winds and tides are the main energy sources for internal waves in the global ocean (Ferrari & Wunsch, 2009), while isolated buoyant plumes common to glacial fjords have not previously been identified as a wave source. In the ocean, only horizontally-propagating plumes from rivers have been linked to internal wave generation (J. D. Nash & Moum, 2005). In the atmosphere, convective plumes associated with thunderstorms are known to generate internal waves (Clark et al., 1986; Fovell et al., 1992; Lane et al., 2001; Yue et al., 2013). Internal waves are commonly observed in fjords and typically develop from tidal flows over sills (Farmer & Smith, 1978; Farmer & Armi, 1999; Gillibrand & Amundrud, 2007; Bourgault et al., 2011; Ross et al., 2014). Very recent observations from the Antarctic Peninsula suggest that iceberg calving events are also a source of internal waves and significant mixing (Meredith et al., 2022).

Propagating internal waves have an upper frequency limit equal to the local buoyancy frequency, N, which ranges from around 24 cycles per day (cpd) in the deep ocean to well over 100 cpd in highly-stratified locations, such as fjords. Winds and tides typically excite waves at frequencies much lower than N (≤ 2 cpd), while nonlinear wave-wave interactions facilitate energy transfers to higher frequencies. In the laboratory, plumes and mechanically-generated turbulence have been demonstrated to generate near-N waves (Dohan & Sutherland, 2005; Ansong & Sutherland, 2010).

While internal gravity waves are ubiquitous in stratified fluids, they have not been observed near the ice-ocean interface of tidewater glaciers. This is due in part to the difficulty involved in collecting measurements close to the calving termini of glaciers, which must be done using autonomous or remotely-operated platforms. Furthermore, moving instruments tend to alias temporal and spatial signals, making it difficult to detect propagating waves. Moored instruments anchored to the seafloor are better able to isolate oscillatory signals but are at significant risk of being destroyed by icebergs and are typically deployed from ships that cannot approach close to glacier termini. Past moored records have been located greater than 1 km from glacier termini, and have generally aimed

for long-duration records, necessitating low-frequency sampling that may not detect high-frequency waves (Moffat, 2014; Jackson et al., 2014).

Here, we present the first-ever time series of ocean velocity within the calving zone of a tidewater glacier. Our observations reveal that energetic internal waves account for nearly half of the near-terminus velocity variability and could significantly enhance melt rates. We are able to reproduce the wave characteristics accurately in an idealised numerical simulation forced only by a subglacial discharge plume. Because discharge plumes are a ubiquitous feature of tidewater glacier systems, such internal waves may be common.

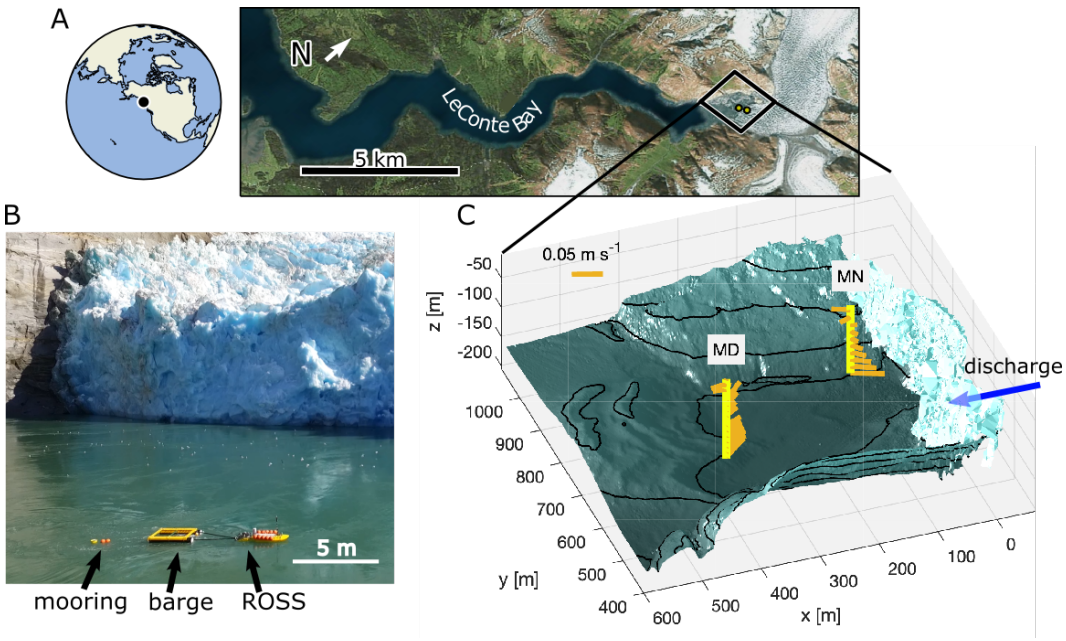

Figure 1. A) Map of LeConte Bay, located in Southeast Alaska. The study region is located at the end of the bay in the boxed region. B) Remote deployment of a mooring captured from drone footage. C) A 3-D view of the observed bathymetry and glacier morphology looking down at the fjord from the southwest. Mooring locations are denoted by yellow bars and mean velocity vectors are given by orange quivers. The approximate location of the discharge outlet is indicated with an arrow.

2 Materials and Methods

In September 2018, an extensive dataset of near-terminus ocean properties were collected during a field campaign at LeConte Glacier (Xeitl Sít' in Tlingit), Alaska (Fig. 1 A). Remotely-controlled kayaks called Robotic Oceanographic Surface Samplers or ROSS (J. Nash et al., 2017) were used to deploy a mooring approximately 100 m from the terminus and roughly 150 m from the discharge plume source (the near mooring, MN, Fig. 1 B & C) at the beginning of the campaign (1–3 Sept). Uniquely, MN was instrumented with a 5 beam Acoustic Doppler Current Profiler (ADCP) providing direct measurements of vertical velocity over 13–134-m depth. A second more distant mooring (denoted MD), instrumented with two 4 beam ADCPs, was deployed by ship approximately 400 m from the terminus and discharge plume, and measured velocities from 6–165-m depth. A series of processing steps are applied to the ADCP data to remove noise, exclude iceberg calving events, and reduce biases, but some of horizontal velocity estimates are likely bi-

ased low due to beam spreading (text S2). Both moorings were recovered at the end of the campaign (12–18 Sept), during which time a large number of additional observations were obtained, including ship- and ROSS-based profiles of temperature and salinity.

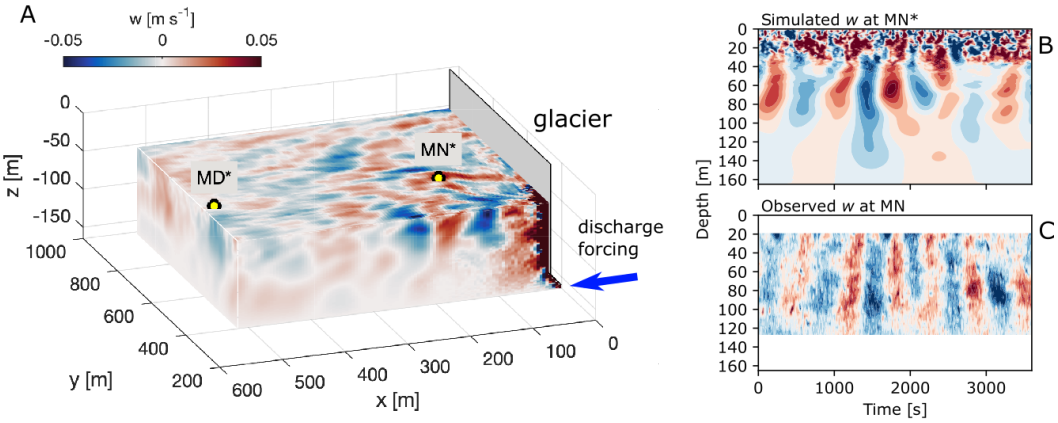

Figure 2. A) A snapshot of the vertical velocity field from a 600 m wide subset of the 1000 m wide large eddy simulation domain. The simulation was forced by 150 m^3 s^{-1} of freshwater injected at the location of the blue arrow. MD* and MN* represent points in the model corresponding to the real mooring locations. B) One hour of vertical velocity output from MN in the large eddy simulation. C) Observed vertical velocity over one hour from mooring MN.

Complementing the in-situ observations, a large eddy simulation (LES) with a uniform resolution of 1 m was conducted to investigate plume-driven ocean variability (Fig. 2 A). Compared to models that have previously been used to study discharge plumes, such as MITgcm, the LES uses a sophisticated turbulence closure scheme that better represents the largest turbulent scales relevant to internal wave generation (text S3). The domain is an idealized rectangular channel of width 1 km, length 6 km, and depth 165 m, approximating the dimensions of the near-terminus region at LeConte. At the eastern wall of the model (the 'glacier') melting is parameterized using the 3-equation model (Holland & Jenkins, 1999). The model was initialized with a horizontally uniform, depth-dependant temperature $T(z)$ and salinity $S(z)$, and forced by 150 m^3 s^{-1} of subglacial discharge injected from a 100 m wide by 4 m high channel at the base of the eastern wall. The temperature and salinity profiles were derived from the average of 35 near-glacier CTD casts. The chosen discharge flux is close to the average for the fieldwork period (Jackson et al., 2020) and the shape of the discharge outlet is roughly based on prior inferences of subglacial outlets from glaciers in Greenland (Jackson et al., 2017; Slater et al., 2017; Fried et al., 2019). Boundary conditions at the western downstream fjord exit above 60 m depth were set to a constant outflow equal to the total prescribed subglacial discharge influx. Below 60 m, the outflow velocity was set to zero.

3 Results

Observed and simulated vertical velocity time series confirm the presence of an energetic internal wave field (Fig. 2). The waves appear as regular bands of positive and negative vertical velocity with a period of approximately 10 minutes and magnitude exceeding 5 cm s^{-1}. The same regular oscillations are also observed in horizontal veloc-

ity and at the more distant mooring (text S4, Fig. S2). An analysis of the dynamical wave modes using observations suggests that the dominant horizontal wavelength lies between 100–800 m, most likely towards the lower end of this range (text S5, Fig. S3). In the numerical simulation, waves emerge from the discharge plume and propagate throughout the fjord and along the terminus (Fig. 2 A, movie S1).

The observed wave signals are superposed on a slowly-varying horizontal circulation (e.g. Fig. 1 C) and turbulent motions confined to the upper 30 m associated with the outflowing discharge plume. The magnitude of observed horizontal velocities is less than the internal waves velocities at mid-depths (30–100-m) but exceeds the wave velocities in the shallowest and deepest parts of the water column (Fig. S2 A & B). Variability in the surface horizontal velocity been analyzed in prior works using iceberg tracking and autonomous boat surveys (Kienholz et al., 2019; Jackson et al., 2020). The turbulent motions are readily seen in the numerical model output (Fig. 2 B), but are not always apparent in the ADCP data because of the instruments' resolution and the potential for surface contamination.

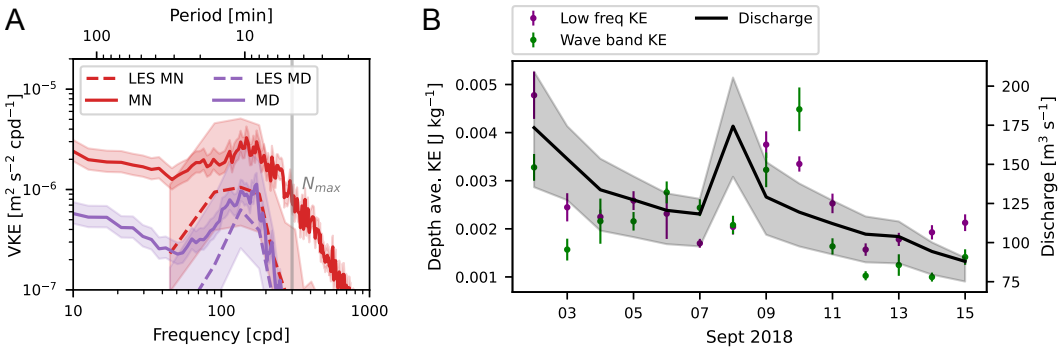

Figure 3. A) Vertical kinetic energy spectra averaged over 30–60-m depth, where the wave signal is strongest, from mooring data (solid lines) and LES (dashed lines). Maximum buoyancy frequency is marked with a vertical line. B) Daily depth-averaged kinetic energy from mooring MN split into wave and low frequency components, as well as the subglacial discharge flux. In all plots the shaded regions and error bars indicate 95% confidence intervals.

Internal waves produce a peak in the vertical kinetic energy spectrum between frequencies of 50–300 cycles per day (cpd) equivalent to 5–30 min periods (Fig. 3 A), close to but less than the maximum observed buoyancy frequency which is ∼300 cpd. We exploit the narrow-band nature of the wave signal to study the relative energy content of waves and their impact on predicted melt rates. Specifically, we decompose the data into a high-frequency wave band (50–300 cpd), and a low-frequency band ($<$ 50 cpd) using moving averages that are robust to data gaps. The wave band isolates the most energetic internal waves but may also contain contributions from non-wave motions such as turbulence at shallow depths. The low-frequency band contains the fjord circulation, as well as low-frequency internal wave motions and tides.

The mean total kinetic energy (KE) in the wave band at mooring MN is (2.1±0.2)$\times$ 10^{-3} J kg^{-1} at 95% confidence or 42 ± 2% of the total when averaged over 20–120 m depth. The depth range chosen is the intersection of the observed depths at the two moorings allowing for a fair comparison at these two locations. At MD, which is 4 times further from the discharge source, the depth-average kinetic energy in the wave band is (0.9± 0.1) $\times$ 10^{-3} J kg^{-1}, approximately half that found at MN.

Internal waves appear near-continuously throughout the observational period but with some variability in their kinetic energy (Fig. 3 B). We find a positive correlation (0.4±0.2 at 68% confidence) between wave KE at the near-glacier mooring and the subglacial discharge flux estimated from a glacier runoff model (Sutherland et al., 2019; Amundson et al., 2020). We also find a positive correlation between low-frequency KE and discharge (0.5 ± 0.2). The short record length, inherent variability in the wave and low-frequency fields, and uncertainty in the runoff model may be reasons for the modest correlation estimates. Times of greater low-frequency KE, such as Sept. 9–11, are associated with the presence of a strong surface outflow of subglacial discharge plume water above the mooring. Prior work has demonstrated that this outflow is often concentrated in a relatively narrow current that regularly changes orientation (Kienholz et al., 2019). The relative timing of peaks in discharge and KE hint at a 1–2 day lag between changes in runoff and changes in ocean circulation (Fig. 3 B), which could result from inadequate representation of water storage in the glacier runoff model (Jansson et al., 2003; Jackson et al., 2022). However, a lag-correlation analysis did not result in higher correlation estimates. Interestingly, we find a good correlation between wave and low-frequency kinetic energy (0.7 ± 0.1), which could indicate that waves derive their energy from the laterally spreading surface expression of the discharge plume, rather than its vertically rising part. Since both the rising and spreading parts ultimately derive their KE from the potential energy of the freshwater ejected at the glacier grounding line, this points to discharge as the common energy source for both low-frequency and wave band KE.

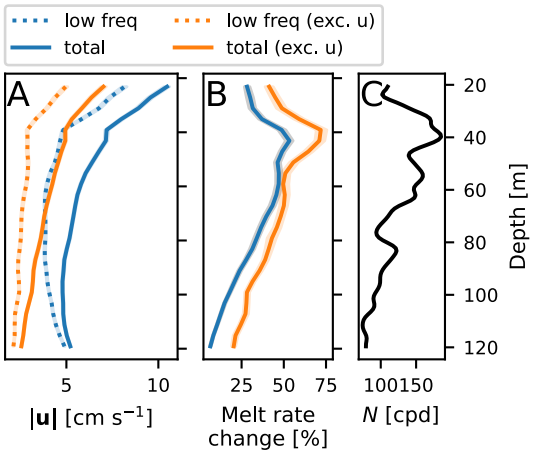

Figure 4. A) Time-mean ocean speed at mooring MN with (solid) and without (dashed) the internal wave band. The speed is calculated in two ways: with the eastward component of velocity (blue) and without (orange). B) Change in parameterized melt rate implied by the inclusion of wave velocities. Shading indicates the 95% confidence interval calculated using a bootstrapping procedure. C) Average buoyancy frequency from 35 near-terminus CTD profiles.

We use Eq. (1) to estimate the impact of high-frequency internal wave motions on melt rates for velocity observations at mooring MN. We estimate terminus-parallel speed in two ways, 1) using only the northward horizontal velocity component, since the glacier terminus is oriented approximately north-south and 2) using all horizontal velocity components (Fig. 4 A). Changes in melt rate are calculated as the ratio of speed with and without high-frequency motions. We neglect the contribution of ambient melt plumes to the velocity, since they were not measured. In both cases, the terminus-parallel mean speed is much greater when wave motions are included. For the 'northward only' case, predicted melt rates above 100-m depth increase by up to 70% (Fig. 4 B), while for the 'northward and eastward' case, they increase by up to 50%. The enhancement in melt

rates is focused around the pycnocline, where buoyancy frequency is greatest (Fig. 4 C), consistent with the expectation from classical internal wave theory that internal wave energy scales with buoyancy frequency (Gill, 1984, Chapter 8.12.2).

4 Discussion

These new measurements from autonomously-deployed moorings suggest that energetic internal waves are a persistent feature at LeConte Glacier. Our results raise a number of questions. How ubiquitous are internal waves at tidewater glaciers? Can you predict wave amplitudes and frequency from subglacial discharge rates and ocean stratification? Tackling these broader questions will be the goal of future work. Below, we focus on two of the main questions that arise from our results, namely, how are the waves generated and what is their potential contribution to melting?

4.1 How are the internal waves generated?

A mechanism for wave generation must explain the properties of the waves found above, in particular, their near-N frequency, persistence and correlations with discharge forcing. Possible mechanisms for generating internal waves include iceberg calving (Meredith et al., 2022), flow-topography interactions (Farmer & Armi, 1999), and turbulent emission (Dohan & Sutherland, 2005). The latter mechanism may occur when turbulent eddies in the discharge plume and its surface expression excite internal waves. While calving and flow-topography interactions may generate waves and introduce variability into measurements, the numerical simulation, which lacks any of these forcings, is able to reproduce the observed wave characteristics. Calving and flow-topography interactions also cannot explain the observed correlation between waves, low-frequency kinetic energy and subglacial discharge fluxes and the persistence of the wave field during periods of low calving activity.

We suggest that a turbulent emission mechanism may best reflect the observations. While traditional theories for discharge plumes cannot generate unsteady waves because they average out unsteady (turbulent) dynamics (Morton et al., 1956), plumes are known to be highly turbulent. Laboratory results have shown that turbulence and buoyant plumes can generate internal waves with a frequency near N (Dohan & Sutherland, 2005; Ansong & Sutherland, 2010). Additionally, the mechanism provides a dynamical connection between turbulence, horizontal fjord circulation, and internal waves that could explain the persistence of waves and the correlation among these quantities. Significantly more work is needed to confirm our suspected mechanism and to better understand high-frequency internal waves at glaciers. While we attempted to eliminate calving induced waves in our data processing, some events may have been missed. Confirmation of a turbulent generation mechanism would require an analysis of energy transfers between turbulence and internal waves, which is beyond the scope of this paper. Additionally, wave properties may depend on non-ocean factors such as discharge outlet geometry and terminus geometry which also vary in time.

4.2 How do internal waves contribute to boundary layer heat and salt fluxes?

Within the 3-equation parameterization, the melt rate is proportional to the ocean boundary layer heat and salt fluxes, which are assumed to be linearly dependent on the terminus-parallel ocean velocity (Eq. (1) and text S1). We consider that the outer velocity may be comprised of plume, mean horizontal and internal wave components denoted by subscript p, subscript m and subscript w respectively, giving,

$$\boldsymbol{u} = (u_m + u_w, 0, w_p + w_w). \tag{2}$$

We have chosen a coordinate system were the second component of velocity is perpendicular to the ice and must satisfy the no-flow condition at the ice-ocean boundary ($v_m = v_w = v_p = 0$) and we neglect the horizontal plume velocity ($u_p = 0$). The contribution of internal waves, plumes and mean flows to melt is the average magnitude of Eq. (2) over a wave period T_w, e.g.

$$m \propto \overline{|\boldsymbol{u}|} = \frac{1}{T_w} \int_0^{T_w} \sqrt{(u_m + u_w)^2 + (w_p + w_w)^2} dt. \tag{3}$$

The nonlinearity of Eq. (3) ensures that waves always contribute to melting. The significance of the wave contribution will depend on the relative magnitude of waves, plumes and mean flows. Within the discharge plume, large vertical velocities associated with buoyantly rising fluid will dominate other velocity sources ($w_p \gg w_w, u_m, u_w$) and the wave contribution may be negligible. In ambient regions far away from the discharge plume, our observations suggest that waves and mean flows have similar magnitude and both contribute to melting ($w_w \sim u_w \sim u_m$). For the case of a single sinusoidally varying wave superposed onto a mean flow with $w_w = u_w = u_m$, Eq. (3) predicts a 30% increase in the melt rate relative to the case without a wave. In our analysis of melt rate enhancement by waves, we did not include the ambient melt plume velocity since it was not measured, which is equivalent to assuming that $w_p \ll w_w$. In the absence of external flow, this assumption is valid since coupled plume-melt theory predicts weak ambient plume velocities of order 1 cm s^{-1} or less, much weaker than the observed wave velocities (Jackson et al., 2020).

The interaction of plumes, mean flows and waves may involve additional complexities that are not captured by the simplified theory presented here. For instance, enhancement of melt by waves and mean flows might provide additional buoyancy to ambient plumes, increasing their vertical velocity. The combination of a mean and oscillatory boundary layer forcing also occurs in the shallow coastal ocean when currents and surface gravity waves both impinge on the seafloor. In this case, the interaction of surface waves and currents with the bottom boundary layer leads to a higher drag coefficient (Trowbridge & Lentz, 2018, and reference therin). If a similar interaction were to occur at the ice-ocean boundary, it suggests another possible mechanism for increased melt rates via an increased drag coefficient.

Wave-induced melting is likely greatest close to the plume and decreases farther away due to spreading of wave energy. However, complicated glacier geometry could lead to focusing or shadowing in certain regions. Our results suggest that wave energy is concentrated at the pycnocline depth. Consequently, numerical models that do not resolve internal waves may underestimate melting around the pycnocline. In many deep glacial-fjord systems, discharge plumes reach neutral buoyancy below the surface. Atmospheric studies and laboratory tests demonstrate that plumes radiate waves upward into stratified regions implying that discharge-generated waves should also be found close to deep termini (Fovell et al., 1992; Lane et al., 2001; Ansong & Sutherland, 2010; Yue et al., 2013). An uneven vertical distribution of melting, as implied by Fig. 4 A and implied by the observed melt rates and geometries collected previously in May 2017 (Sutherland et al., 2019), may also lead to uneven glacier shapes that are more prone to calving (Slater et al., 2021). The observed profile of terminus-parallel velocity increases in magnitude toward the surface and could cause melt-induced overcutting, in agreement with observed Sept. 2018 ice morphology (Abib et al., n.d., in review).

5 Conclusion

Our observations reveal the presence of an energetic internal wavefield at Xeitl Sít' (LeConte Glacier). Analyses confirm these are generated by the subglacial discharge plume

and have the potential to significantly enhance melt rates. Because the fundamental ingredients needed to excite these waves are common to most tidewater glacier systems – an energetic upwelling plume impinging on a stratified ocean – we expect the waves to be widely prevalent at other tidewater glaciers in Greenland, Alaska and Patagonia. Prior laboratory studies suggest that the internal wave energy flux scales with the plume energy flux (Ansong & Sutherland, 2010) suggesting that more energetic waves may be found at tidewater glaciers with higher discharge rates and more energetic plumes. Our findings highlight the importance of obtaining measurements very close to glaciers, since observations taken far away may miss key dynamical processes and greatly underestimate the energy of ocean flows that can enhance melting. Ultimately, the impact of high-frequency internal waves should be included in parameterizations of melt for accurate modeling of ocean-glacier interactions.

Open Research Section

The oceanographic data (ship, autonomous vessel, moorings) are archived at the National Centers for Environmental Information (Accession 0189574, accession.nodc.noaa.gov/0189574). The glacier (subglacial discharge) data have been archived at the Arctic Data Center (doi.org/10.18739/A22G44). The analysis code is available on GitHub (github.com/jessecusack/LeConte_plume_internal_waves) and will be archived with Zenodo upon publication of this manuscript.

Acknowledgments

These observations were made possible by the talented engineering team who developed the remotely operated vessels and mooring deployment system: Jasmine Nahorniak, June Marion, Nick McComb, Anthony Grana, and Corwin Perren, as well as the Captain and crew of the M/V Amber Anne. We acknowledge the generosity of Teledyne RD Instruments for lending a Sentinel V ADCP despite significant risk of loss. JMC acknowledges the support of a Rutgers EOAS postdoctoral fellowship. This work was supported by NSF OPP Grants 1503910, 1504191, 1504288, 1504521, 2023269, 2023319, and 2023674. ONR grants N00014-14-1-0490 and N00014-17-1-2864 supported autonomous vessel development. The National Geographic Society Grant CP4-171R-17 supported the design and deployment of the novel system to remotely deploy moorings. We would like to acknowledge high-performance computing support from Cheyenne (doi:10.5065/D6RX99HX) provided by NCAR's Computational and Information Systems Laboratory, sponsored by NSF.

References

Abib, N., Sutherland, D. A., Amundson, J. M., Duncan, D., Jackson, R. H., Kienholz, C., & Morlighem, M. (n.d.). Persistent overcut regions dominate the terminus morphology of a rapidly melting tidewater glacier. *Annals of Glaciology*, 41.

Amundson, J. M., Kienholz, C., Hager, A. O., Jackson, R. H., Motyka, R. J., Nash, J. D., & Sutherland, D. A. (2020). Formation, flow and break-up of ephemeral ice mélange at LeConte Glacier and Bay, Alaska. *Journal of Glaciology*, *66*(258), 577–590. doi: 10.1017/jog.2020.29

Ansong, J. K., & Sutherland, B. R. (2010, April). Internal gravity waves generated by convective plumes. *Journal of Fluid Mechanics*, *648*, 405–434. doi: 10.1017/S0022112009993193

Bourgault, D., Janes, D. C., & Galbraith, P. S. (2011, March). Observations of a Large-Amplitude Internal Wave Train and Its Reflection off a Steep Slope. *Journal of Physical Oceanography*, *41*(3), 586–600. doi: 10.1175/2010JPO4464.1

Carroll, D., Sutherland, D. A., Hudson, B., Moon, T., Catania, G. A., Shroyer, E. L., ... van den Broeke, M. R. (2016). The impact of glacier geometry on meltwater plume structure and submarine melt in Greenland fjords. *Geophysical Research Letters*, *43*(18), 9739–9748. doi: 10.1002/2016GL070170

Chambers, D. P., Cazenave, A., Champollion, N., Dieng, H., Llovel, W., Forsberg, R., ... Wada, Y. (2017). Evaluation of the Global Mean Sea Level Budget between 1993 and 2014. *Surveys in Geophysics*, *38*(1), 309–327. doi: 10.1007/s10712-016-9381-3

Clark, T. L., Hauf, T., & Kuettner, J. P. (1986, October). Convectively forced internal gravity waves: Results from two-dimensional numerical experiments. *Quarterly Journal of the Royal Meteorological Society*, *112*(474), 899–925. doi: 10.1002/qj.49711247402

Cowton, T., Slater, D., Sole, A., Goldberg, D., & Nienow, P. (2015, February). Modeling the impact of glacial runoff on fjord circulation and submarine melt rate using a new subgrid-scale parameterization for glacial plumes. *Journal of Geophysical Research: Oceans*, *120*(2), 796–812. doi: 10.1002/2014JC010324

Dohan, K., & Sutherland, B. R. (2005). Numerical and laboratory generation of internal waves from turbulence. *Dynamics of Atmospheres and Oceans*, *40*(1-2 SPEC. ISS.), 43–56. doi: 10.1016/j.dynatmoce.2004.10.004

Farmer, D., & Armi, L. (1999, September). Stratified flow over topography: The role of small-scale entrainment and mixing in flow establishment. *Proceedings of the Royal Society of London. Series A: Mathematical, Physical and Engineering Sciences*, *455*(1989), 3221–3258. doi: 10.1098/rspa.1999.0448

Farmer, D., & Smith, J. D. (1978, January). Nonlinear Internal Waves in a Fjord. In J. C. J. Nihoul (Ed.), *Elsevier Oceanography Series* (Vol. 23, pp. 465–493). Elsevier. doi: 10.1016/S0422-9894(08)71294-7

Ferrari, R., & Wunsch, C. (2009, January). Ocean Circulation Kinetic Energy: Reservoirs, Sources, and Sinks. *Annual Review of Fluid Mechanics*, *41*(1), 253–282. doi: 10.1146/annurev.fluid.40.111406.102139

Fovell, R., Durran, D., & Holton, J. R. (1992, August). Numerical Simulations of Convectively Generated Stratospheric Gravity Waves. *Journal of the Atmospheric Sciences*, *49*(16), 1427–1442. doi: 10.1175/1520-0469(1992)049⟨1427:NSOCGS⟩2.0.CO;2

Fried, M. J., Carroll, D., Catania, G. A., Sutherland, D. A., Stearns, L. A., Shroyer, E. L., & Nash, J. D. (2019). Distinct Frontal Ablation Processes Drive Heterogeneous Submarine Terminus Morphology. *Geophysical Research Letters*, *46*(21), 12083–12091. doi: 10.1029/2019GL083980

Fried, M. J., Catania, G. A., Bartholomaus, T. C., Duncan, D., Davis, M., Stearns, L. A., ... Sutherland, D. (2015). Distributed subglacial discharge drives significant submarine melt at a Greenland tidewater glacier. *Geophysical Research Letters*, *42*(21), 9328–9336. doi: 10.1002/2015GL065806

Gill, A. E. (1984). On the Behavior of Internal Waves in the Wakes of Storms. *Journal of Physical Oceanography*, *14*(7), 1129–1151. doi: 10.1175/1520-0485(1984)014⟨1129:otboiw⟩2.0.co;2

Gillibrand, P. A., & Amundrud, T. L. (2007). A numerical study of the tidal circulation and buoyancy effects in a Scottish fjord: Loch Torridon. *Journal of Geophysical Research: Oceans*, *112*(C5). doi: 10.1029/2006JC003806

Holland, D. M., & Jenkins, A. (1999, August). Modeling Thermodynamic Ice–Ocean Interactions at the Base of an Ice Shelf. *Journal of Physical Oceanography*, *29*(8), 1787–1800. doi: 10.1175/1520-0485(1999)029⟨1787:MTIOIA⟩2.0.CO;2

Jackson, R. H., Motyka, R. J., Amundson, J. M., Abib, N., Sutherland, D. A., Nash, J. D., & Kienholz, C. (2022). The Relationship Between Submarine Melt and Subglacial Discharge From Observations at a Tidewater Glacier. *Journal of Geophysical Research: Oceans*, *127*(10), e2021JC018204. doi: 10.1029/2021JC018204

Jackson, R. H., Nash, J. D., Kienholz, C., Sutherland, D. A., Amundson, J. M., Motyka, R. J., ... Pettit, E. C. (2020). Meltwater Intrusions Reveal Mechanisms for Rapid Submarine Melt at a Tidewater Glacier. *Geophysical Research Letters*, *47*(2). doi: 10.1029/2019GL085335

Jackson, R. H., Shroyer, E. L., Nash, J. D., Sutherland, D. A., Carroll, D., Fried, M. J., ... Stearns, L. A. (2017). Near-glacier surveying of a subglacial discharge plume: Implications for plume parameterizations. *Geophysical Research Letters*, *44*(13), 6886–6894. doi: 10.1002/2017GL073602

Jackson, R. H., Straneo, F., & Sutherland, D. A. (2014, July). Externally forced fluctuations in ocean temperature at Greenland glaciers in non-summer months. *Nature Geosci*, *7*(7), 503–508. doi: 10.1038/ngeo2186

Jansson, P., Hock, R., & Schneider, T. (2003, November). The concept of glacier storage: A review. *Journal of Hydrology*, *282*(1-4), 116–129. doi: 10.1016/S0022-1694(03)00258-0

Jenkins, A. (2011). Convection-driven melting near the grounding lines of ice shelves and tidewater glaciers. *Journal of Physical Oceanography*, *41*(12), 2279–2294. doi: 10.1175/JPO-D-11-03.1

Kienholz, C., Amundson, J. M., Motyka, R. J., Jackson, R. H., Mickett, J. B., Sutherland, D. A., ... Truffer, M. (2019). Tracking icebergs with time-lapse photography and sparse optical flow, LeConte Bay, Alaska, 2016-2017. *Journal of Glaciology*, *65*(250), 195–211. doi: 10.1017/jog.2018.105

Lane, T. P., Reeder, M. J., & Clark, T. L. (2001, May). Numerical Modeling of Gravity Wave Generation by Deep Tropical Convection. *Journal of the Atmospheric Sciences*, *58*(10), 1249–1274. doi: 10.1175/1520-0469(2001)058⟨1249:NMOGWG⟩2.0.CO;2

Luckman, A., Benn, D. I., Cottier, F., Bevan, S., Nilsen, F., & Inall, M. (2015). Calving rates at tidewater glaciers vary strongly with ocean temperature. *Nature Communications*, *6*. doi: 10.1038/ncomms9566

Ma, Y., & Bassis, J. N. (2019, February). The Effect of Submarine Melting on Calving From Marine Terminating Glaciers. *Journal of Geophysical Research: Earth Surface*, *124*(2), 334–346. doi: 10.1029/2018JF004820

MacKinnon, J. A., Alford, M. H., Ansong, J. K., Arbic, B. K., Barna, A., Briegleb, B. P., ... Zhao, Z. (2017, March). Climate Process Team on Internal-Wave Driven Ocean Mixing. *Bulletin of the American Meteorological Society*, BAMS-D-16-0030.1. doi: 10.1175/BAMS-D-16-0030.1

Magorrian, S. J., & Wells, A. J. (2016, July). Turbulent plumes from a glacier terminus melting in a stratified ocean. *Journal of Geophysical Research: Oceans*, *121*(7), 4670–4696. doi: 10.1002/2015JC011160

McConnochie, C. D., & Kerr, R. C. (2017, July). Testing a common ice-ocean parameterization with laboratory experiments. *Journal of Geophysical Research: Oceans*, *122*(7), 5905–5915. doi: 10.1002/2017JC012918

Melet, A., Hallberg, R., Legg, S., & Polzin, K. (2013, March). Sensitivity of the Ocean State to the Vertical Distribution of Internal-Tide-Driven Mixing. *Journal of Physical Oceanography*, *43*(3), 602–615. doi: 10.1175/JPO-D-12-055.1

Mercenier, R., Lüthi, M. P., & Vieli, A. (2020, April). How Oceanic Melt Controls Tidewater Glacier Evolution. *Geophysical Research Letters*, *47*(8), 1–9. doi: 10.1029/2019GL086769

Meredith, M. P., Inall, M. E., Brearley, J. A., Ehmen, T., Sheen, K., Munday, D., ... Scourse, J. (2022, November). Internal tsunamigenesis and ocean mixing driven by glacier calving in Antarctica. *Science Advances*, *8*(47), 1–11. doi: 10.1126/sciadv.add0720

Moffat, C. (2014). Wind-driven modulation of warm water supply to a proglacial fjord, Jorge Montt Glacier, Patagonia. *Geophysical Research Letters*, *41*(11), 3943–3950. doi: 10.1002/2014GL060071

Morton, B., Taylor, G., & Turner, J. S. (1956, January). Turbulent gravitational

convection from maintained and instantaneous sources. *Proceedings of the Royal Society of London. Series A. Mathematical and Physical Sciences*, *234*(1196), 1–23. doi: 10.1098/rspa.1956.0011

Mouginot, J., Rignot, E., Bjørk, A. A., van den Broeke, M., Millan, R., Morlighem, M., ... Wood, M. (2019). Forty-six years of Greenland Ice Sheet mass balance from 1972 to 2018. *Proceedings of the National Academy of Sciences of the United States of America*, *116*(19), 9239–9244. doi: 10.1073/pnas.1904242116

Nash, J., Marion, J., McComb, N., Nahorniak, J., Jackson, R., Perren, C., ... Lee, S. (2017, June). Autonomous CTD Profiling from the Robotic Oceanographic Surface Sampler. *Oceanography*, *30*(2), 110–112. doi: 10.5670/oceanog.2017.229

Nash, J. D., & Moum, J. N. (2005). River plumes as a source of large-amplitude internal waves in the coastal ocean. *Nature*, *437*(7057), 400–403. doi: 10.1038/nature03936

Rignot, E., Fenty, I., Xu, Y., Cai, C., & Kemp, C. (2015). Undercutting of marine-terminating glaciers in West Greenland. *Geophysical Research Letters*, *42*(14), 5909–5917. doi: 10.1002/2015GL064236

Rignot, E., & Kanagaratnam, P. (2006). Changes in the velocity structure of the Greenland Ice Sheet. *Science*, *311*(5763), 986–990. doi: 10.1126/science.1121381

Ross, L., Pérez-Santos, I., Valle-Levinson, A., & Schneider, W. (2014, December). Semidiurnal internal tides in a Patagonian fjord. *Progress in Oceanography*, *129*, 19–34. doi: 10.1016/j.pocean.2014.03.006

Schulz, K., Nguyen, A. T., & Pillar, H. R. (2022, September). An Improved and Observationally-Constrained Melt Rate Parameterization for Vertical Ice Fronts of Marine Terminating Glaciers. *Geophysical Research Letters*, *49*(18). doi: 10.1029/2022GL100654

Shepherd, A., Ivins, E., Rignot, E., Smith, B., van den Broeke, M., Velicogna, I., ... The IMBIE Team (2020, March). Mass balance of the Greenland Ice Sheet from 1992 to 2018. *Nature*, *579*(7798), 233–239. doi: 10.1038/s41586-019-1855-2

Slater, D. A., Benn, D. I., Cowton, T. R., Bassis, J. N., & Todd, J. A. (2021). Calving Multiplier Effect Controlled by Melt Undercut Geometry. *Journal of Geophysical Research: Earth Surface*, *126*(7), 1–17. doi: 10.1029/2021JF006191

Slater, D. A., Carroll, D., Oliver, H., Hopwood, M. J., Straneo, F., Wood, M., ... Morlighem, M. (2022). Characteristic Depths, Fluxes, and Timescales for Greenland's Tidewater Glacier Fjords From Subglacial Discharge-Driven Upwelling During Summer. *Geophysical Research Letters*, *49*(10), e2021GL097081. doi: 10.1029/2021GL097081

Slater, D. A., Nienow, P., Sole, A., Cowton, T., Mottram, R., Langen, P., & Mair, D. (2017). Spatially distributed runoff at the grounding line of a large Greenlandic tidewater glacier inferred from plume modelling. *Journal of Glaciology*, *63*(238), 309–323. doi: 10.1017/jog.2016.139

Slater, D. A., Nienow, P. W., Cowton, T. R., Goldberg, D. N., & Sole, A. J. (2015, April). Effect of near-terminus subglacial hydrology on tidewater glacier submarine melt rates. *Geophysical Research Letters*, *42*(8), 2861–2868. doi: 10.1002/2014GL062494

Slater, D. A., Straneo, F., Das, S. B., Richards, C. G., Wagner, T. J., & Nienow, P. W. (2018). Localized Plumes Drive Front-Wide Ocean Melting of A Greenlandic Tidewater Glacier. *Geophysical Research Letters*, *45*(22), 12,350–12,358. doi: 10.1029/2018GL080763

Straneo, F., & Cenedese, C. (2015). The dynamics of greenland's glacial fjords and their role in climate. *Annual Review of Marine Science*, *7*(August 2014), 89–112. doi: 10.1146/annurev-marine-010213-135133

Sutherland, D. A., Jackson, R. H., Kienholz, C., Amundson, J. M., Dryer, W. P.,

Supporting Information for "Internal gravity waves generated by subglacial discharge: implications for tidewater glacier melt"

J. M. Cusack[1,2], R. H. Jackson[2], J. D. Nash[1], E. Skyllingstad[1], E. C. Pettit[1],

D. A. Sutherland[3], R. J. Motyka[4,5], J M. Amundson[5]

[1]Oregon State University, College of Earth, Ocean and Atmospheric Sciences

[2]Rutgers, The State University of New Jersey

[3]University of Oregon

[4]University of Alaska Fairbanks

Contents of this file

1. Text S1 to S5

2. Figures S1 to S3

Additional Supporting Information (Files uploaded separately)

1. Caption for Movie S1

Introduction

The supporting information explains the theoretical underpinnings of the 3-equation melt parameterization (S1), and details the configuration of the moored instruments and

the large eddy simulation (S2 & S3). It also contains additional examples of observed velocity from the moorings (S4), and details on wavelength estimation method and results (S5).

S1. The 3-Equation Model

The 3-equation model describes the thermodynamics of ice melting into seawater, such as the base of an ice shelf or the terminus of a tidewater glacier (Holland & Jenkins, 1999; Jenkins, 2011). Importantly, the model parameterizes the turbulent and diffusive fluxes of heat and salt through the ocean boundary layer. The first equation in the model describes the dependence of the ice-ocean interface temperature T_b, which must remain at the freezing point, on depth, z, and interface salinity S_b,

$$T_b = \lambda_1 S_b + \lambda_2 + \lambda_3 z, \tag{1}$$

where the coefficients $\lambda_{1,2,3}$, are empirical and arise from a linearization of the equation for the freezing point temperature (IOC et al., 2010).

The remaining two equations in the model represent the balance of heat (superscript T) and salt (superscript S) at the interface,

$$Q^T = Q_I^T - Q_M^T, \tag{2}$$

$$Q^S = -Q_M^S, \tag{3}$$

where, Q^T is the latent heat of melting, Q_I^T is the heat flux through the ice, Q_M^T is the heat flux through the ocean boundary layer, Q^S is the salt (freshwater) flux due to melting, and Q_M^S is the salt (freshwater) flux through the ocean boundary layer. Physically, the first

equation states that the latent heat of melting is supplied by the difference in heat fluxes through the ice and ocean boundary layer. The second equation states that freshwater released by melting is fluxed through the ocean boundary layer to maintain the interface at the salinity dependent freezing point temperature.

The ocean boundary layer fluxes in Eqs. 2 - 3 (terms with subscript M) depend on viscous-diffusive and turbulent flows of very small scales that are not resolved by most numerical models or captured in most observations. When turbulence in the boundary layer arises from the shear instability of flows external to the boundary layer, such as discharge plumes, internal waves or the mean circulation, the heat and salt equations may be written as,

$$m[c_i(T_b - T_i) - L] = c_w C_D^{\frac{1}{2}} \Gamma_T |\boldsymbol{u}|(T - T_b), \tag{4}$$

$$mS_b = C_D^{\frac{1}{2}} \Gamma_S |\boldsymbol{u}|(S - S_b). \tag{5}$$

where the right-hand sides parameterize the ocean fluxes assuming a linear dependence on the ice-parallel ocean speed outside the boundary layer $|\boldsymbol{u}|$. Other variables represent: the melt rate m, the heat capacity of ice c_i, the ice temperature T_i, the latent heat of melting L, the heat capacity of water c_w, the drag coefficient C_D, the ocean salinity outside the boundary layer S, the ocean temperature outside the boundary layer T, the turbulent transfer coefficient for heat Γ_T, and the turbulent transfer coefficient for salt Γ_S. For a given ice temperature, ocean temperature, ocean salinity and ocean velocity Eqs. (1), (4) and (5) may be solved for the melt rate. The form of the parameterization has been

validated in the laboratory for ocean velocities greater than 4 cm s^{-1} (McConnochie & Kerr, 2017), a condition that is easily met at LeConte Glacier.

S2. Moorings and ADCP processing

Two moorings instrumented with one or more Acoustic Doppler Current Profilers (ADCP, Fig. S1) were used for these analyses. The near-glacier mooring (MN, 56.8370392 N, 132.3574123 W) consisted of an upward looking Teledyne RDI Sentinal V 300 kHz ADCP located at 134 m, measuring to 13 m depth, sampling every 2.5 s with 4 m vertical resolution. At the distant mooring (MD, 56.83596667 N, 132.3616833 W), one upward looking Teledyne RDI 300 kHz Workhorse was located at 84 m depth and second downward looking Workhorse was placed at 86 m, providing coverage between 165 - 6 m with 3 m resolution. Both ADCPs sampled every 1.75 s.

Individual ping data were averaged into 10 s bins prior to analysis. Noisy data were rejected when the correlation metric, a measure of the signal to noise ratio, was less than 60 %. An additional fraction of the shallowest and deepest data were removed due to side lobe contamination from the surface and bottom. The fraction removed was equal to $1-\cos(\theta)$, where θ is the ADCP beam angle from vertical. The beam angle is typically 20 - 25° and results in a 6 - 10 % data loss. Sediment settling produced a spurious downward velocity that was particularly apparent when the outflowing plume was located above a mooring (horizontal velocity estimates were unaffected). The wave band filter (5 to 30 min period) effectively removes slowly varying sediment biases; however, some short period sediment fluctuations may still remain. Sporadic iceberg calving events kicked up

impulsive flows of short duration that are not the focus of this study. These time periods were removed from the dataset using an instrument pitch/roll threshold.

The design of traditional ADCPs, which combine along-beam velocity measurements from several beams to estimate Earth coordinate velocity (e.g. Fig. S1), may bias wave observations when the wavelength of the wave is comparable to or smaller than the beam separation. The bias scales with distance from the instrument, d, as $\cos(k_h d \tan(\theta))$, where k_h is the horizontal wavenumber (inverse wavelength $k_h = \frac{2\pi}{\lambda}$) of the wave under observation and θ is the beam angle from vertical. The bias is small for long waves where $k_h d \sim 0$ but can be significant for short waves. We estimate that 150 m wavelength waves are essentially invisible to the ADCPs for distances around 70 m. As such, our estimates of wave energy are likely biased low. The Sentinel V instrument (mooring MN) has a vertical beam lacking such a bias, from which reliable estimates of vertical velocity were obtained. Nevertheless, horizontal velocity may be significantly biased, particularly in the upper water column. The bias is less significant at mooring MD since two ADCPs were located at mid-depth such that $k_h d$ is smaller.

S3. Large eddy simulation

The non-hydrostatic, rotating, Boussinesq fluid equations are integrated in time using the large eddy simulation described in Skyllingstad, Smyth, Moum, and Wijesekera (1999) and Skyllingstad, Smyth, and Crawford (2000) based on the Deardorff (1980) equation set with subgrid scale turbulence closure from Ducros, Comte, and Lesieur (1996). The complex bathymetry of LeConte Bay was idealized to a rectangular channel of width 1 km, length 6 km and depth 165 m. The grid resolution was set to 1 m in all dimensions in

the 1 km closest to the terminus. Starting at 1 km away from the terminus, the resolution in the along-fjord (x dimension) was gradually increased to 7 m at the domain edge so as to reduce computational cost.

The model was forced by injecting 150 m^3 s^{-1} of freshwater from a 100 m wide by 4 m high channel centered at $y = 400$ m on the base of the eastern wall. While evidence exists for a choice of outlet width (Jackson et al., 2017; Slater et al., 2017; Fried et al., 2019), the outlet height at the point where discharge starts mixing with the ocean is a very poorly constrained parameter. Dynamically, the outlet height sets the initial plume momentum (for fixed width and discharge flux) and plume theory suggests that the initial momentum has little effect on plume properties higher up in the water column (Morton et al., 1956; Jenkins, 2011; Hewitt, 2020). As such, our choice for the height is necessarily arbitrary, but reasonable given the lack of evidence for a particular value.

Constant gradient boundaries were prescribed at the lateral channel walls with outflow velocity set to zero. Zero outflow at the terminus was also prescribed away from the discharge region, with northward and vertical velocity component gradient set using a log similarity profile and assumed ice roughness length of 0.1 m, similar to ice boundary conditions used in Skyllingstad, Paulson, Pegau, McPhee, and Stanton (2003), but more representative of fractured glacial ice. Boundary conditions at the downstream fjord exit above 60 m depth were set to a constant outflow equal to the total prescribed subglacial discharge influx. Below 60 m, the outflow velocity was set to zero. Downstream boundary conditions for all other variables were set to a constant gradient. Velocity conditions at the bottom were also set using a similarity log profile with assumed roughness length of 0.005

m and constant gradient for scalar variables. The upper boundary was approximated as a rigid lid.

The model was initialised with vertically varying temperature and salinity calculated from the mean of 35 CTD profiles in the near-glacier region. It was subsequently run for 4 hours. The total kinetic energy averaged cross-fjord at 500 m from the glacier asymptotes to a quasi-steady value by 1 hour. All analysis of the model presented in this paper is conducted on the last 3 hours of output.

S4. Horizontal velocity and observations from MD

Eastward velocity observed at MN over 1 hr is plotted in Fig. S2 A. The eastward velocity signal exhibits a 10 min period internal-wave-induced fluctuation, similar to that observed in vertical velocity (Fig. 2 C). Other non-wave variability associated with the plume-driven fjord circulation and tides also appear in the horizontal velocity signal, especially at the greatest and shallowest depths.

Internal wave fluctuations in velocity are also observed at the more distant mooring, MD (Fig. S2 B & C). Here, low frequency motions, also associated with the plume-drive fjord circulation, tides and flow over topography, appear in horizontal layers and are stronger than at MN. The vertical velocity fluctuations at MD (Fig. S2 C) are generally slightly weaker than at MN.

S5. Horizontal wavelength

The Taylor-Goldstein (T-G) equation (Taylor, 1931; Goldstein, 1931) is commonly used to study internal wave dynamics when stratification varies with depth. Solutions to the equation comprise a set of vertical modes, which describe the vertical structure of internal

waves and their associated frequencies. We solve the T-G equation for the mean observed density profile (fig. S3 A), assuming no horizontal velocity, using finite difference methods (Smyth et al., 2011) and assess how frequency and mode structure change with horizontal wavenumber (the only free parameter). We only expect to approximately reproduce the observed wave structure, because the exact vertical structure will depend on the details of the density profile and horizontal velocity at any given time.

We find that the vertical structure of the observations are generally consistent with a lowest mode internal wave (having no zero-crossings in vertical velocity) (Fig. S3 B). Moreover, the method suggests an upper bound on the horizontal wavelength of $\sim$ 800 m, corresponding to 30 min period waves (Fig. S3 C). Our spectral analysis suggests that most energy is associated with periods closer to 10 min, which corresponds to a wavelength close to 100 m.

Movie S1. Vertical velocity at 50 m depth as a function of eastward and northward position from the LES. The location of the plume (y = 400 m) is marked with an arrow.

References

Deardorff, J. W. (1980). Stratocumulus-capped mixed layers derived from a three-dimensional model. *Boundary-Layer Meteorology*, *18*(4), 495–527. doi: 10.1007/BF00119502

Ducros, F., Comte, P., & Lesieur, M. (1996). Large-eddy simulation of transition to turbulence in a boundary layer developing spatially over a flat plate. *Journal of Fluid Mechanics*, *326*, 1–36. doi: 10.1017/s0022112096008221

Fried, M. J., Carroll, D., Catania, G. A., Sutherland, D. A., Stearns, L. A., Shroyer, E. L.,

& Nash, J. D. (2019). Distinct Frontal Ablation Processes Drive Heterogeneous Submarine Terminus Morphology. *Geophysical Research Letters*, *46*(21), 12083–12091. doi: 10.1029/2019GL083980

Goldstein, S. (1931, August). On the stability of superposed streams of Fluids of different densities. *Proceedings of the Royal Society of London A*, *132*(820), 524–548. doi: 10.1098/rspa.1931.0116

Hewitt, I. J. (2020). Subglacial Plumes. *Annual Review of Fluid Mechanics*, *52*, 145–169. doi: 10.1146/annurev-fluid-010719-060252

Holland, D. M., & Jenkins, A. (1999, August). Modeling Thermodynamic Ice–Ocean Interactions at the Base of an Ice Shelf. *Journal of Physical Oceanography*, *29*(8), 1787–1800. doi: 10.1175/1520-0485(1999)029⟨1787:MTIOIA⟩2.0.CO;2

IOC, SCOR, & IAPSO. (2010). The international thermodynamic equation of seawater – 2010: Calculation and use of thermodynamic properties. *Intergovernmental Oceanographic Commission, Manuals and Guides No. 56*.

Jackson, R. H., Shroyer, E. L., Nash, J. D., Sutherland, D. A., Carroll, D., Fried, M. J., ... Stearns, L. A. (2017). Near-glacier surveying of a subglacial discharge plume: Implications for plume parameterizations. *Geophysical Research Letters*, *44*(13), 6886–6894. doi: 10.1002/2017GL073602

Jenkins, A. (2011). Convection-driven melting near the grounding lines of ice shelves and tidewater glaciers. *Journal of Physical Oceanography*, *41*(12), 2279–2294. doi: 10.1175/JPO-D-11-03.1

McConnochie, C. D., & Kerr, R. C. (2017, July). Testing a common ice-ocean param-

eterization with laboratory experiments. *Journal of Geophysical Research: Oceans*, *122*(7), 5905–5915. doi: 10.1002/2017JC012918

Morton, B., Taylor, G., & Turner, J. S. (1956, January). Turbulent gravitational convection from maintained and instantaneous sources. *Proceedings of the Royal Society of London. Series A. Mathematical and Physical Sciences*, *234*(1196), 1–23. doi: 10.1098/rspa.1956.0011

Skyllingstad, E. D., Paulson, C. A., Pegau, W. S., McPhee, M. G., & Stanton, T. (2003). Effects of keels on ice bottom turbulence exchange. *Journal of Geophysical Research: Oceans*, *108*(12), 1–16. doi: 10.1029/2002jc001488

Skyllingstad, E. D., Smyth, W. D., & Crawford, G. B. (2000). Resonant wind-driven mixing in the ocean boundary layer. *Journal of Physical Oceanography*, *30*(8), 1866–1890. doi: 10.1175/1520-0485(2000)030⟨1866:RWDMIT⟩2.0.CO;2

Skyllingstad, E. D., Smyth, W. D., Moum, J. N., & Wijesekera, H. (1999). Upper-ocean turbulence during a westerly wind burst: A comparison of large-eddy simulation results and microstructure measurements. *Journal of Physical Oceanography*, *29*(1), 5–28. doi: 10.1175/1520-0485(1999)029⟨0005:UOTDAW⟩2.0.CO;2

Slater, D. A., Nienow, P., Sole, A., Cowton, T., Mottram, R., Langen, P., & Mair, D. (2017). Spatially distributed runoff at the grounding line of a large Greenlandic tidewater glacier inferred from plume modelling. *Journal of Glaciology*, *63*(238), 309–323. doi: 10.1017/jog.2016.139

Smyth, W. D., Moum, J. N., & Nash, J. D. (2011). Narrowband oscillations in the upper equatorial ocean. Part II: Properties of Shear instabilities. *Journal of Physical*

Oceanography, *41*(3), 412–428. doi: 10.1175/2010JPO4451.1

Taylor, G. I. (1931, August). Effect of variation in density on the stability of superposed streams of Fluid. *Proceedings of the Royal Society of London A*, *132*(820), 499–523. doi: 10.1098/rspa.1931.0115

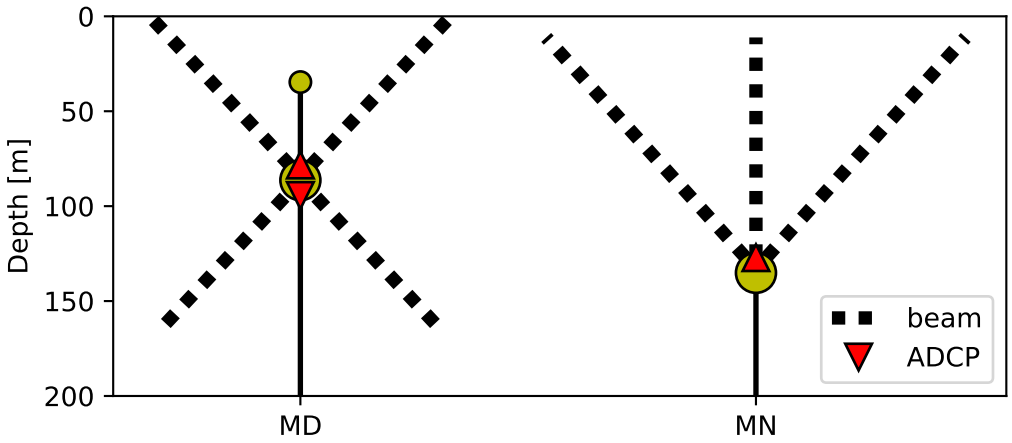

Figure S1. Schematic of moorings MD and MN detailing the location of the ADCPs (red triangles) and divergence of acoustic beams (dashed lines).

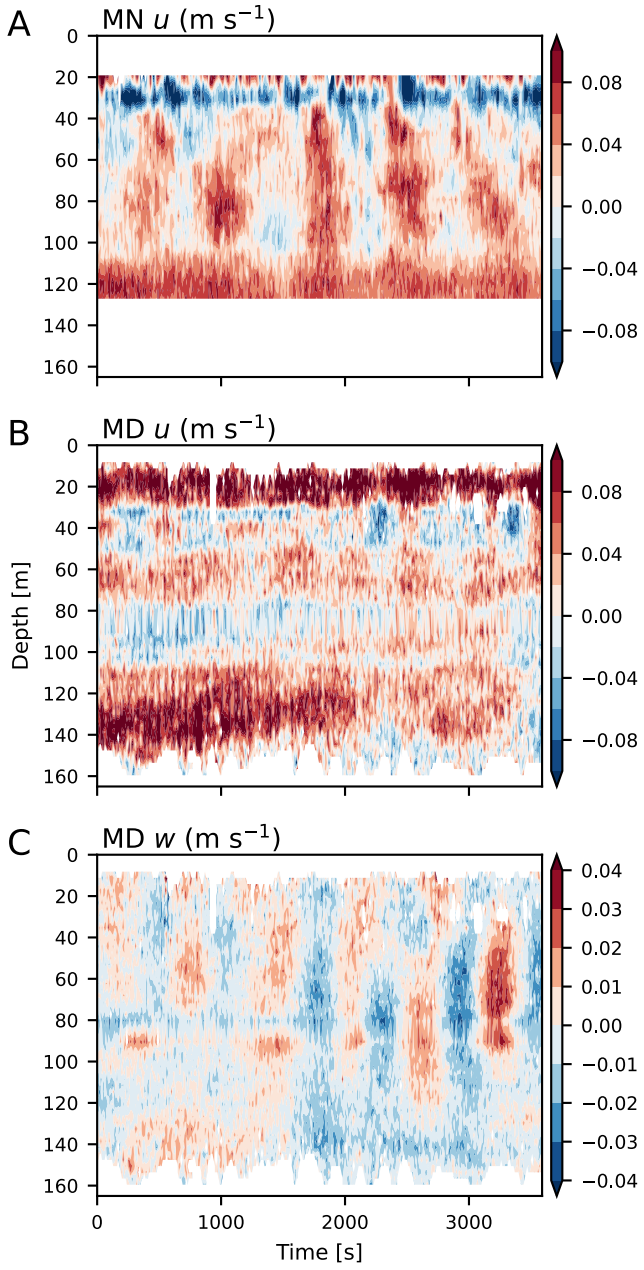

Figure S2. Time series of A) eastward velocity at MN, B) eastward velocity at the MD, and C) vertical velocity at MD. The data plotted here are unfiltered and a subsample of the whole record.

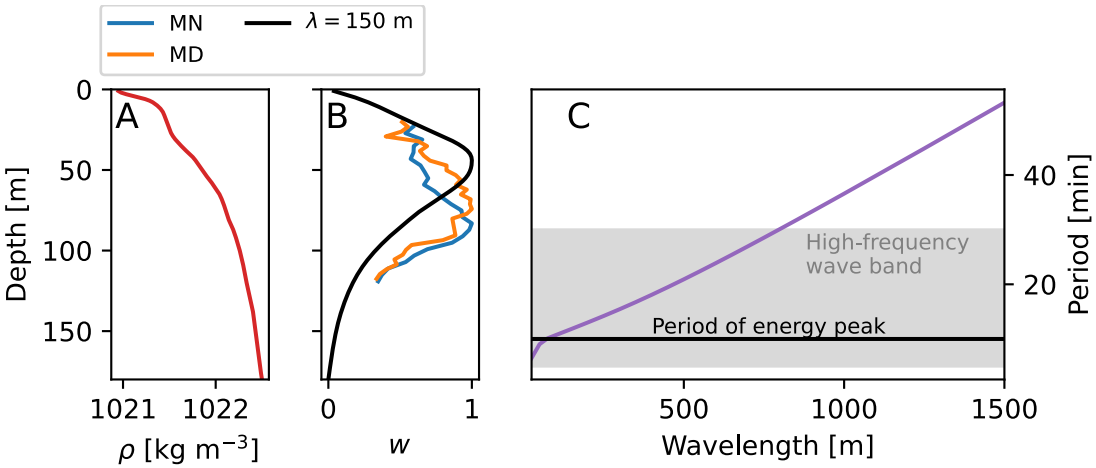

Figure S3. A) Mean potential density from ship and ROSS data. B) The colored lines represent root mean square vertical velocity between 20 - 120 m for the segment of mooring data plotted in Fig. S2. The lowest mode solution of the T-G equation for a wavelength of 150 m is marked in black. Values are normalised so that the maximum equals 1. C) The purple line denotes the lowest mode period as a function of wavelength from the T-G solution. The period of peak wave energy in the observations ($\sim$ 10 min) is marked by the black horiziontal line. The shaded region denotes the high-frequency wave band.

Duncan, D., ... Nash, J. D. (2019). Direct observations of submarine melt and subsurface geometry at a tidewater glacier. *Science*, *365*(6451), 369–374. doi: 10.1126/science.aax3528

Thornalley, D. J., Oppo, D. W., Ortega, P., Robson, J. I., Brierley, C. M., Davis, R., ... Keigwin, L. D. (2018). Anomalously weak Labrador Sea convection and Atlantic overturning during the past 150 years. *Nature*, *556*(7700), 227–230. doi: 10.1038/s41586-018-0007-4

Trowbridge, J. H., & Lentz, S. J. (2018, January). The Bottom Boundary Layer. *Annual Review of Marine Science*, *10*(1), 397–420. doi: 10.1146/annurev-marine-121916-063351

Wood, M., Rignot, E., Fenty, I., Menemenlis, D., Millan, R., Morlighem, M., ... Seroussi, H. (2018). Ocean-Induced Melt Triggers Glacier Retreat in Northwest Greenland. *Geophysical Research Letters*, *45*(16), 8334–8342. doi: 10.1029/2018GL078024

Woodson, C. B. (2018). The fate and impact of internal waves in nearshore ecosystems. *Annual Review of Marine Science*, *10*(August 2017), 421–441. doi: 10.1146/annurev-marine-121916-063619

Yue, J., Hoffmann, L., & Joan Alexander, M. (2013). Simultaneous observations of convective gravity waves from a ground-based airglow imager and the AIRS satellite experiment. *Journal of Geophysical Research: Atmospheres*, *118*(8), 3178–3191. doi: 10.1002/jgrd.50341